



Article

# Predicting the Fate of Bisphenol A During Electrochemical Oxidation: A Simple Semiempirical Method Based on the Concentration Profile of Hydroxyl Radicals

Marija Ječmenica Dučić <sup>1,\*</sup> , Dragana Vasić Anićijević <sup>1</sup> , Danka Aćimović <sup>1</sup> , Ľubomír Švorc <sup>2</sup> ,  
Branko Bugarski <sup>3</sup>, Radojica Pešić <sup>3</sup> and Tanja Brdarić <sup>1</sup>

<sup>1</sup> Department of Physical Chemistry, Vinča Institute of Nuclear Sciences—National Institute of the Republic of Serbia, University of Belgrade, Mike Petrovića Alasa 12–14, 11000 Belgrade, Serbia

<sup>2</sup> Institute of Analytical Chemistry, Faculty of Chemical and Food Technology, Slovak University of Technology in Bratislava, Radlinského 9, 812 37 Bratislava, Slovakia

<sup>3</sup> Department of Chemical Engineering, Faculty of Technology and Metallurgy, University of Belgrade, Karnegijeva 4, 11000 Belgrade, Serbia

\* Correspondence: marija.jecmenica@vin.bg.ac.rs

**Abstract:** The efficiency of electrochemical advanced oxidation processes (EAOPs) is fundamentally governed by hydroxyl-radical ( $\bullet\text{OH}$ ) generation. While direct experimental measurements of these transient species remain complex and impractical, robust computational methods for predicting their temporal profiles are notably scarce. This work presents a semi-empirical methodology based on  $\text{H}_2\text{O}_2$  measuring experiments that enables indirect  $\bullet\text{OH}$  quantification. We employed a recently developed carbon-based electrode and the priority pollutant bisphenol A (BPA) as the model system. The system achieved 92.3% BPA degradation with 84% mineralization efficiency during 5-h electrooxidation at  $15\text{ mA/cm}^2$ . Gas chromatography/mass spectrometry (GC/MS) was used for tracking BPA and detection of intermediates. On this basis, we developed a computational model that successfully predicts temporal concentration profiles of all reactive species interacting with  $\bullet\text{OH}$ , along with degradation kinetics across current densities ( $10\text{--}20\text{ mA/cm}^2$ ). By incorporating predictions from the Toxicity Estimation Software Tool (T.E.S.T.), the developed model accurately simulates time-dependent evolution of relative toxicity throughout the treatment process. The presented approach has a general character and requires rather simple experimental input to predict and optimize degradation outcome in terms of input concentration, degradation time, current density, and final toxicity. Further modifications of the model would enable widening to other EAOPs systems.

**Keywords:** kinetic modelling; bisphenol A (BPA); electrooxidation processes; organic pollutants; second-order rate constants



Academic Editors: Chengdu Qi and Guilong Peng

Received: 15 April 2025

Revised: 8 May 2025

Accepted: 11 May 2025

Published: 16 May 2025

**Citation:** Ječmenica Dučić, M.; Vasić Anićijević, D.; Aćimović, D.; Švorc, Ľ.; Bugarski, B.; Pešić, R.; Brdarić, T. Predicting the Fate of Bisphenol A During Electrochemical Oxidation: A Simple Semiempirical Method Based on the Concentration Profile of Hydroxyl Radicals. *Int. J. Mol. Sci.* **2025**, *26*, 4785. <https://doi.org/10.3390/ijms26104785>

**Copyright:** © 2025 by the authors. Licensee MDPI, Basel, Switzerland. This article is an open access article distributed under the terms and conditions of the Creative Commons Attribution (CC BY) license (<https://creativecommons.org/licenses/by/4.0/>).

## 1. Introduction

Electrochemical advanced oxidation processes (EAOPs) represent a promising and thoroughly investigated set of methods for the removal of organic pollutants in aqueous media [1,2]. During EAOPs, organic pollutants are depleted in interaction with active radicals generated on the electrode surface [3,4]. The type and concentration of radicals responsible for pollutant degradation depend on the electrode material and process conditions [5], and the efficiency of the process is, by the rule, directly proportional to the energy input [6–8]. The electrochemical oxidation is an EAOP method that uses electric current to oxidize organic matter, relying heavily on the generation and reactivity of hydroxyl radicals

( $\bullet\text{OH}$ ) [9–11]. Although other radicals such as hydroperoxyl radicals ( $\text{HO}_2\bullet$ ) and sulfate radicals ( $\text{SO}_4\bullet^-$ ) also take place in sulfate-mediated electrochemical oxidation, the literature data report that their reactivity towards organic molecules is a few orders of magnitude lower compared to  $\bullet\text{OH}$  [12–15]. Superoxide radicals ( $\text{O}_2\bullet^-$ ) also show lower reactivity compared to hydroxyl radicals ( $\bullet\text{OH}$ ) in wastewater treatment oxidation processes [16].

Due to their short lifespan and high reactivity, direct measurements of  $\bullet\text{OH}$  radicals are challenging [17]. Several indirect methods have been developed to detect and quantify these elusive species, each with its own advantages and limitations. These include electron paramagnetic resonance (EPR) spectroscopy and fluorescence spectroscopy, which require complex equipment and are unreliable in oxidizing conditions [18,19]. Chemical dosimetry relies on the chemical reaction of  $\bullet\text{OH}$  with specific probes to form measurable products, also being highly dependent on the probe selectivity and chemical properties of the system in general [19–21].

On the other hand, kinetic modelling provides insight into  $\bullet\text{OH}$  radical concentration and enables understanding of its trends [22–24], once when the kinetics of  $\bullet\text{OH}$  formation and depletion are known in reaction with other species, without external limitations of experimental measurements. They offer a complementary framework for understanding the complex processes governing  $\bullet\text{OH}$  behavior [25], offering the possibility to further optimize experimental parameters while predicting transformation products and treatment efficiency [26]. Integrating experimental data with computational modeling enables the design of electrochemical systems for efficient and environmentally responsible pollutant degradation. Although it is generally accepted that active radicals should be considered when modelling degradation processes, studies involving general kinetic modelling of their concentration distribution during EAOPs remain scarce [27,28]. Existing research has primarily focused on photocatalytic UV/ $\text{H}_2\text{O}_2$  systems [29,30], with particular attention to the degradation of pharmaceuticals [31–33], while highlighting the need to develop new models for compounds beyond dyes [34]. This gap is especially critical for harmful and ubiquitous priority pollutants that resist removal through conventional wastewater treatment methods and whose degradation bears the risk of the formation of potentially toxic by-products [35,36]. For these persistent contaminants, predicting both water toxicity and degradation product concentrations becomes particularly important [37]. In this view, semiempirical modelling of  $\bullet\text{OH}$  radical behavior based on some simple experimental input is of particular interest, considering its universal role in EAOPs and AOPs in general.

For the reaction of the target organic pollutant with the  $\bullet\text{OH}$  radical (Equation (1)), the general elementary second-order rate law can be written as the expression in Equation (2), where  $[\text{Pollutant}]_t$  and  $[\bullet\text{OH}]_t$  are the time-dependent concentrations of pollutant and  $\bullet\text{OH}$  radical, and  $k_{\bullet\text{OH}}^{\text{pollutant}}$  is a pseudo-second-order (i.e., binary or absolute) rate constant.



$$\text{rate} = -\frac{d[\text{Pollutant}]_t}{dt} = k_{\bullet\text{OH}}^{\text{pollutant}} [\bullet\text{OH}]_t [\text{Pollutant}]_t \quad (2)$$

In bulk solution, the effective concentration of  $\bullet\text{OH}$  radicals available to degrade organic pollutants is affected by a number of coupled phenomena, such as electrode surface processes, adsorption, diffusion, and mixing [38,39]. Moreover, since  $\bullet\text{OH}$  radicals are non-selective reactive species, they interact with the target organic pollutant, reaction intermediates and by-products, scavengers, and even with each other in recombination reactions, all causing  $[\bullet\text{OH}]_t$  to vary during the degradation process in a more or less complex manner [40].

In summary, the effective  $\bullet\text{OH}$  radical concentration [41], acts as a specific characteristic for a particular electrode: a specific electrode generates a certain amount of  $\bullet\text{OH}$  radicals, which, under the same transport conditions, leads to  $[\bullet\text{OH}]_t$  proportional to the applied current density  $j$  ( $\text{mA}/\text{cm}^2$ ).

Given the foregoing, there has been the need to develop a kinetic model that predicts the concentration profile of  $\bullet\text{OH}$  radicals at different current densities, as a characteristic of a specific electrode, using simple experimental parameters as the input data. Once defined, the model would enable prediction of concentration distribution of pollutants and degradation intermediates depending on degradation time and current density. Moreover, known distribution of intermediates provides input for predicting related quantities of interest, such as degradation extent or total toxicity of the reaction mixture, when the toxicity parameters of the reaction intermediates are known.

This study employed bisphenol A (BPA), a well-characterized endocrine disruptor [42–45], as a model pollutant. While BPA degradation has been extensively studied in various advanced oxidation processes (e.g., photooxidation [46], catalytic wet air oxidation [36,47]), this work focuses on electrochemical oxidation using a  $\text{SnO}_2\text{-MWCNT@SS}$  anode (tin oxide-modified multi-walled carbon nanotubes on stainless steel). All experimental data were generated using this specifically synthesized electrode, whose morphological and electrochemical properties were thoroughly characterized in our prior studies [48,49]. Mechanistic investigations [50–52] confirm that this composite anode mediates BPA degradation primarily via  $\bullet\text{OH}$  radicals in sulfate media with a pH of 4–7 [53,54]. While BPA degradation—addressing process efficiency and operational parameters such as applied current density—were recently investigated in detail [49], a systematic analysis of intermediates formed during 5-h BPA electrooxidation has not been performed yet.

The aim of the present study was to bridge the required experimental gaps and integrate experimental data with kinetic modeling in order to predict concentration profiles and related quantities (degradation efficiency, degree of mineralization, and the toxicity of the sample during degradation) depending on given reaction parameters, such as current density and degradation time. To address the challenge of measuring  $\bullet\text{OH}$  radicals necessary to obtain second-order rate constants, a strategy was to estimate  $[\bullet\text{OH}]_t$  using data on an easily measurable concentration of  $\text{H}_2\text{O}_2$  which are in equilibrium with  $\bullet\text{OH}$  radicals. A proposed approach was applied to the anodic oxidation of BPA using a  $\text{SnO}_2\text{-MWCNT@SS}$  electrode under a current density of  $15 \text{ mA}/\text{cm}^2$ . Experimental data on BPA degradation intermediates were collected using gas chromatography/mass spectrometry (GC/MS) analysis. The developed model was validated using data on BPA degradation at different current densities with the  $\text{SnO}_2\text{-MWCNT@SS}$  electrode [49] and employed to predict time-dependent toxicity trends in the investigated degradation mixture. To evaluate its broader applicability to diverse organic pollutants, we further validated the model using rhodamine B degradation data obtained with the same  $\text{SnO}_2\text{-MWCNT@SS}$  electrode system [48].

## 2. Results

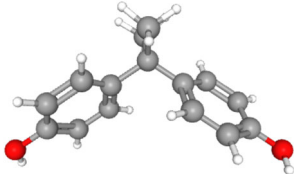
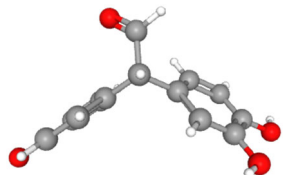
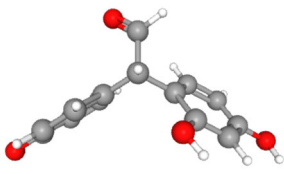
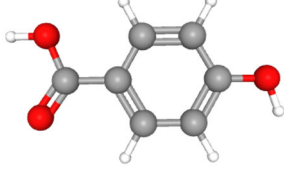
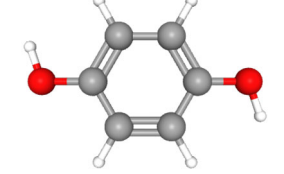
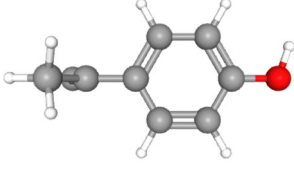
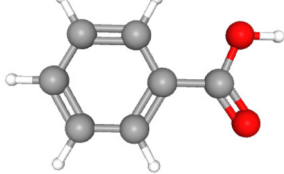
### 2.1. Determination of Bisphenol A (BPA) Degradation Intermediates

The anode modeled in this study was comprehensively characterized in our prior work, including its synthesis procedure, structural/morphological properties, electrochemical performance, stability, and recyclability [48,49].

GC/MS analysis identified derivatized (silylated) intermediates during five-hour BPA electrolysis at  $15 \text{ mA}/\text{cm}^2$ . Compound identification combined mass-to-charge ratios ( $m/z$ ), characteristic ion fragmentation spectra from GC/MS analysis, and molecular formula matching using the NIST reference library [55]. This approach revealed six reactive

intermediates, whose acute toxicities were quantified as 96-h LC<sub>50</sub> values for *Pimephales promelas* (Fathead Minnow), as documented in Table 1.

**Table 1.** Organic compounds identified by gas chromatography/mass spectrometry (GC/MS) during 5 h of bisphenol A (BPA) electrooxidation using a tin oxide-modified multi-walled carbon nanotubes on stainless steel anode (SnO<sub>2</sub>-MWCNT@SS).

Compound Name	Structural Formula [56]	Retention Time (min)	Molar Mass (g/mol)	96-h LC <sub>50</sub> Fathead Minnow (mg/L)
Bisphenol A C <sub>15</sub> H <sub>16</sub> O <sub>2</sub>		23.15	228.29	3.24
Product A 2-(3,4-dihydroxyphenyl)-2-(4-hydroxyphenyl)acetaldehyde C <sub>14</sub> H <sub>12</sub> O <sub>4</sub>		24.33	244.24	1.83
Product B 2-(2,4-dihydroxyphenyl)-2-(4-hydroxyphenyl)acetaldehyde C <sub>14</sub> H <sub>12</sub> O <sub>4</sub>		24.05	244.24	2.26
4-hydroxybenzoic acid C <sub>7</sub> H <sub>6</sub> O <sub>3</sub>		16.5	138.12	92.62
Hydroquinone C <sub>6</sub> H <sub>6</sub> O <sub>2</sub>		13.45	110.11	43.29
4-isopropenylphenol C <sub>9</sub> H <sub>10</sub> O		12.9	140.22	7.67
Benzoic Acid C <sub>7</sub> H <sub>6</sub> O <sub>2</sub>		11.1	122.12	101.5

All detected organic compounds have had aromatic structure, including either two aromatic rings or one ring, suggesting that oxidation of BPA begins at the 1-propane site, subsequently leading to the cleavage of ortho-positioned C-C bonds. While aliphatic interme-

diates were not detected—possibly due to the aromatic-targeted extraction method—their presence is inferred from the observed 84% mineralization efficiency (Table S2). Temporal evolution of relative intensities (peak area) for detected BPA degradation intermediates during the 5-h electrooxidation at 15 mA/cm<sup>2</sup> is provided in Figure 1.

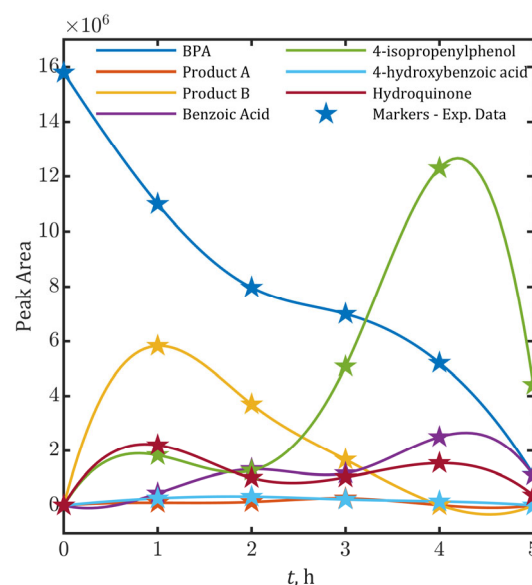


**Figure 1.** Temporal evolution of peak areas for bisphenol A (BPA) degradation intermediates during electrooxidation at 15 mA/cm<sup>2</sup>. Star markers (★) represent experimental data points.

The results align with recent electro-Fenton (EF) studies of the same system under identical conditions [57]. While both processes reached high final efficiencies (EF: 96.3% BPA removal, 89% mineralization; electrooxidation, EO: 92.3% BPA removal, 84% mineralization), the kinetic advantage of EF was pronounced in the early stages of treatment. For example, at the 3-h mark, EF achieved 85.87% BPA degradation (vs. 68.24% for EO) and 79% mineralization (vs. 41.2% for EO).

## 2.2. Kinetic Model Framework

Based on previous results, we assumed the following steps in the degradation kinetics: (i) second-order •OH-driven BPA degradation ( $k_s$ , Equation (3)) forms  $P_{tr}$  (lumped two-ring products); (ii)  $P_{tr}$  undergoes •OH-induced cleavage to one-ring  $P_{or}$  ( $k_B$ , Equation (4)); and (iii) direct mineralization of  $P_{or}$  ( $k_M$ , Equation (5)) was assumed, as aliphatic intermediates were undetected by GC/MS (though implied by organic matter removal (TOC) results). These assumptions are consistent with previous findings that BPA degradation produces numerous intermediates through complex, competing pathways [58–60].

The kinetic model resolves the governing relationships of •OH generation and interconversion, where •OH radicals recombine to form H<sub>2</sub>O<sub>2</sub>. Equation (6) represents the fundamental recombination equilibrium between •OH and H<sub>2</sub>O<sub>2</sub> during anodic water electrolysis [14]. This equilibrium gives rise to Equation (7), which quantifies their competitive formation dynamics. Most significantly, the equilibrium position enables back-calculation of transient •OH concentrations from experimentally measured H<sub>2</sub>O<sub>2</sub> levels (Equation (8)). Collectively, these equations establish a quantitative framework to characterize the electrode's operational •OH yield the critical driver of the degradation mechanisms outlined in Equations (3)–(5).





Differential rate laws were applied to describe  $\bullet OH$ -involving reactions: BPA depletion (Equation (9)),  $P_{tr}$  depletion (Equation (10)),  $P_{or}$  depletion (Equation (11)), and  $CO_2$  evolution (Equation (12)). Equation (13) expresses the mass balance for the system, where  $[BPA]_0$  represents the initial BPA concentration. This conservation law ensures full carbon accounting throughout the electrooxidation process. As experimental observations confirmed that  $\bullet OH$ -mediated oxidation overwhelmingly surpassed adsorptive processes, the adsorption of BPA on the electrode was considered negligible and was not included in the model (Supplementary Materials Text S1 and Table S1). The complete data processing methodology and normalization procedures are detailed in Supplementary Materials (Text S2).

$$k_1 \cdot [\bullet OH]_t \cdot [\bullet OH]_t = k_2 \cdot [H_2O_2]_t \quad (7)$$

$$[\bullet OH]_t = \text{constant} \cdot \sqrt{[H_2O_2]_t} \quad (8)$$

$$\frac{d[BPA]_t}{dt} = -k_S \cdot [BPA]_t \cdot [\bullet OH]_t \quad (9)$$

$$\frac{d[P_{tr}]_t}{dt} = k_S \cdot [BPA]_t \cdot [\bullet OH]_t - k_B \cdot [P_{tr}]_t \cdot [\bullet OH]_t \quad (10)$$

$$\frac{d[P_{or}]_t}{dt} = k_B \cdot [P_{tr}]_t \cdot [\bullet OH]_t - k_M \cdot [P_{or}]_t \cdot [\bullet OH]_t \quad (11)$$

$$\frac{d[CO_2]_t}{dt} = k_M \cdot [P_{or}]_t \cdot [\bullet OH]_t \quad (12)$$

$$[BPA]_0 = [BPA]_t + [P_{tr}]_t + [P_{or}]_t + [CO_2]_t \quad (13)$$

To ensure robust parameter estimation, we implemented a normalization scheme where concentrations were normalized as  $[i]^* = [i]_t / [BPA]_0$  (for  $i = BPA, P_{tr}, P_{or}, CO_2, \bullet OH, H_2O_2$ ) and time was scaled as  $t^* = t / (1 \cdot 10^{-6} \text{ s})$  to avoid optimization convergence issues (Equation (14)). The resulting dimensionless equations (Equations (15)–(20)) enabled estimation of four key parameters: the proportionality factor  $k$ , and dimensionless rate constants  $k_S^*$ ,  $k_B^*$  and  $k_M^*$  (constrained to 0–1 range to avoid optimization pitfalls).

$$\frac{d[i]^*}{dt^*} = \frac{d([i]_t / [BPA]_0)}{d(t / \text{scaling factor})} = \frac{\text{scaling factor}}{[BPA]_0} \cdot \frac{d[i]_t}{dt} \quad (14)$$

$$\frac{d[BPA]^*}{dt^*} = -k_S^* \cdot [BPA]^* \cdot [\bullet OH]^* \quad (15)$$

$$\frac{d[P_{tr}]^*}{dt^*} = k_S^* \cdot [BPA]^* \cdot [\bullet OH]^* - k_B^* \cdot [P_{tr}]^* \cdot [\bullet OH]^* \quad (16)$$

$$\frac{d[P_{or}]^*}{dt^*} = k_B^* \cdot [P_{tr}]^* \cdot [\bullet OH]^* - k_M^* \cdot [P_{or}]^* \cdot [\bullet OH]^* \quad (17)$$

$$\frac{d[CO_2]^*}{dt^*} = k_M^* \cdot [P_{or}]^* \cdot [\bullet OH]^* \quad (18)$$

$$[BPA]^* + [P_{tr}]^* + [P_{or}]^* + [CO_2]^* = 1 \quad (19)$$

$$[\bullet OH]^* = \frac{\text{constant}}{\sqrt{[BPA]_0}} \cdot \sqrt{[H_2O_2]^*} = k \cdot \sqrt{[H_2O_2]^*} \quad (20)$$

Absolute rate constants ( $k_S$ ,  $k_B$  and  $k_M$ ) were subsequently derived through scaling relationships (Equation (21)). All kinetic parameters were estimated in time units of seconds, consistent with standard rate constant conventions ( $1/(M \cdot s)$ ). This normalized kinetic framework provides a comprehensive description of the anodic oxidation process while maintaining numerical stability during parameter optimization.

$$k_j = \frac{k_j^*}{(\text{scaling factor} \cdot [BPA]_0)} \quad (21)$$

### 2.3. Hydroxyl Radical Concentration Dynamics from $H_2O_2$ Experimental Measurements

The hydrogen peroxide time evolution measurement was used to calculate hydroxyl radical concentration, according to Equation (20). The relative concentrations of BPA and  $H_2O_2$ , monitored hourly during 5-h degradation experiments at  $15 \text{ mA/cm}^2$ , are represented in Figure 2.

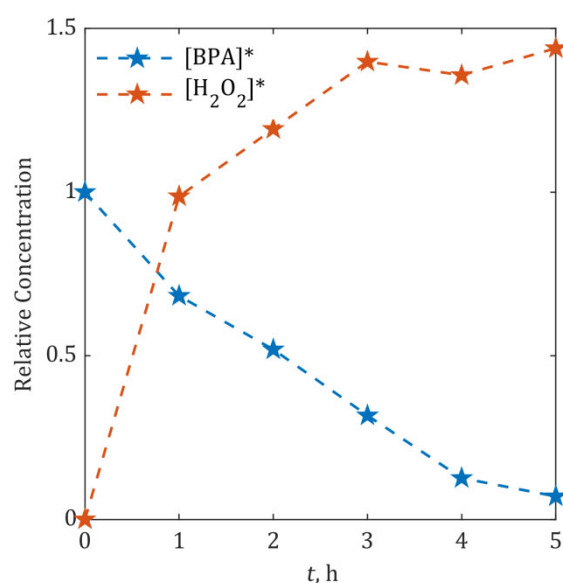


**Figure 2.** Measured relative BPA and  $H_2O_2$  concentrations ( $[BPA]^*$  and  $[H_2O_2]^*$ ) during 5-h anodic oxidation at  $15 \text{ mA/cm}^2$  ( $SnO_2$ -MWCNT@SS anode). Asterisk (\*) denotes normalized concentration.

In order to derive the time concentration profile of the  $\bullet OH$  radical, the  $H_2O_2$  concentration data were fitted by a polynomial. A third-order polynomial (Equation (22)) yielded the optimal fit for the experimental data in Figure 2 ( $R^2 = 0.977$ ), with coefficients:  $B_0 = 3.09 \cdot 10^{-2}$ ,  $B_1 = 3.39 \cdot 10^{-4} \text{ 1/s}$ ,  $B_2 = -3.10 \cdot 10^{-8} \text{ 1/s}^2$  and  $B_3 = 8.81 \cdot 10^{-13} \text{ 1/s}^3$ . The fitted curve is shown in Figure S1.

$$f(t) = \sqrt{[H_2O_2]^*} = B_0 + B_1 \cdot t + B_2 \cdot t^2 + B_3 \cdot t^3 \implies [\bullet OH]^* = k \cdot (B_0 + B_1 \cdot t + B_2 \cdot t^2 + B_3 \cdot t^3) \quad (22)$$

For initial estimation of the proportionality factor  $k$ , we used the literature-reported second-order rate constant for BPA reaction with  $\bullet OH$  radicals ( $1 \cdot 10^{10} \text{ 1/(M} \cdot \text{s)}$ ) for all three kinetic constants ( $k_S$ ,  $k_B$  and  $k_M$ ) [61–63]. The optimal  $k$  value ( $1 \cdot 10^{-10}$ ) was determined by minimizing the discrepancy between model-predicted  $[BPA]^*$  and experimental data in Figure 2. Results of optimization are represented in Figure 3a. Alternative simulations using  $k$  values differing by orders of magnitude are provided in Figure S2. This sensitivity analysis (Figure S2) revealed  $k$  with  $\pm 1$  order-of-magnitude variation causing  $>50\%$  deviation in  $[BPA]^*$  predictions.



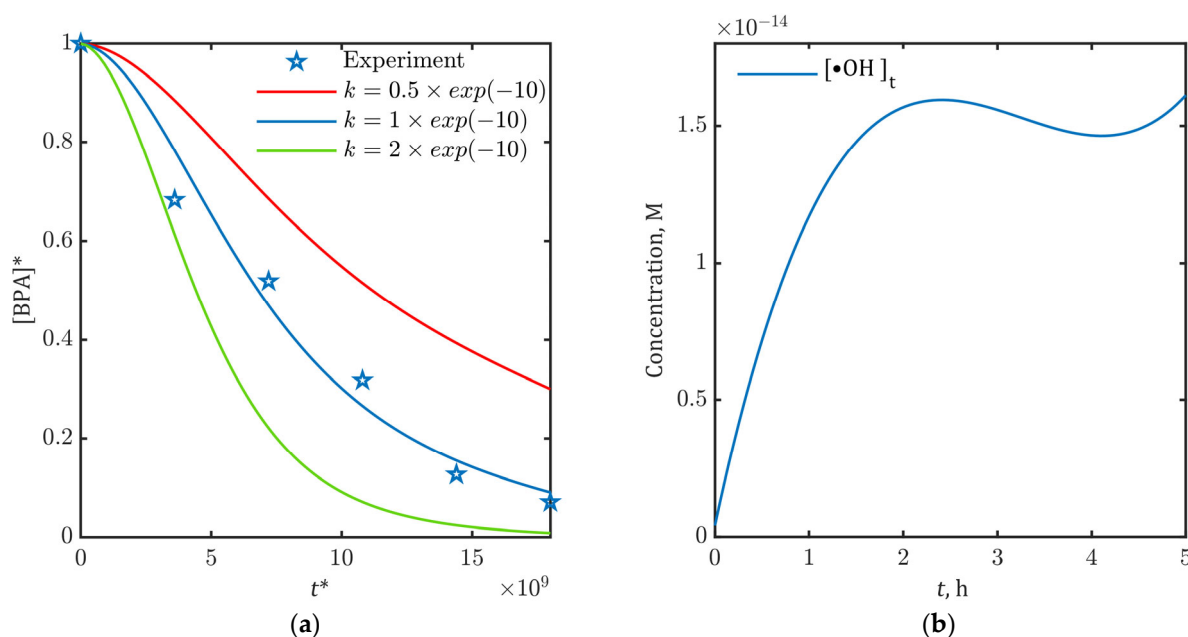


**Figure 3.** (a) Model-predicted relative BPA concentrations ( $[BPA]^*$ ) for varying proportionality factors ( $k$ ). Asterisk (\*) indicates normalized variables; (b) Hydroxyl radical ( $•OH$ ) concentration profile during BPA electrooxidation at 15 mA/cm<sup>2</sup> (SnO<sub>2</sub>-MWCNT@SS anode).

The kinetic model enabled the prediction of time-dependent  $•OH$  concentrations through Equation (23), using the optimized proportionality factor ( $k = 1 \times 10^{-10}$ ). Figure 3b presents the simulated  $•OH$  profile during BPA electrooxidation at 15 mA/cm<sup>2</sup>, showing characteristic rapid initial generation in the first two hours followed by a quasi-steady-state behavior.

$$[•OH]^* = k \cdot \left( B_0 + B_1 \cdot t^* \cdot \text{scaling factor} + B_2 \cdot (t^* \cdot \text{scaling factor})^2 + B_3 \cdot (t^* \cdot \text{scaling factor})^3 \right) \quad (23)$$

#### 2.4. Determination of Second-Order Rate Constants via Kinetic Modelling

The proposed kinetic model (Equations (15)–(20)), incorporating  $[•OH]^*$  estimated from Equation (23), was fitted to the experimental temporal profiles of BPA and its degradation intermediates (Figure 1) to determine the second-order rate constants ( $k_S$ ,  $k_B$  and  $k_M$ ). Parameter estimation yielded the following rate constants (95% confidence intervals):  $k_S = (10.02 \pm 1.19) \cdot 10^9$  1/(M · s) (Equation (3)),  $k_B = (3.92 \pm 1.48) \cdot 10^{10}$  1/(M · s) (Equation (4)) and  $k_M = (13.87 \pm 2.64) \cdot 10^9$  1/(M · s) (Equation (5)). The model demonstrated robust predictive performance, as evidenced by the overall statistical profile: high goodness-of-fit ( $R^2 = 0.980$  for BPA degradation efficiency and  $R^2 = 0.996$  for mineralization efficiency, i.e., CO<sub>2</sub> formation), low prediction errors (RMSE = 0.039, 3.9% relative error), and minimal residual variance (RSS = 0.0105). A complete statistical profile is provided in Table S3 (Supplementary Materials). The notably reduced determination coefficients for  $P_{tr}$  ( $R^2 = 0.828$ ) and  $P_{or}$  ( $R^2 = 0.677$ ) are attributed to the lumping approach used in the kinetic model, which combines intermediates with inherently distinct polarity and oxidation kinetics. This variability is reflected in the estimated 95% confidence interval for the composite rate constant  $k_B = (3.92 \pm 1.48) \cdot 10^{10}$  1/(M · s), confirming that the observed deviations originate from grouping species with differing individual oxidation rates rather than model inadequacy. Consequently, the precision of the prediction of concentrations of intermediates could be further increased by improving the precision of experimental analysis that was used to determine input concentrations of intermediates.



The close agreement between simulated and experimental concentration profiles (Figure 4) provides strong validation of both the proposed  $\bullet\text{OH}$ -driven reaction mechanism and the accuracy of parameter estimation methodology, confirming model reliability across the entire 5-h process. Predicted  $\bullet\text{OH}$  concentrations (Figure 3b) and rate constants also aligned well with literature values for analogous systems [64–66], confirming the model's mechanistic plausibility.

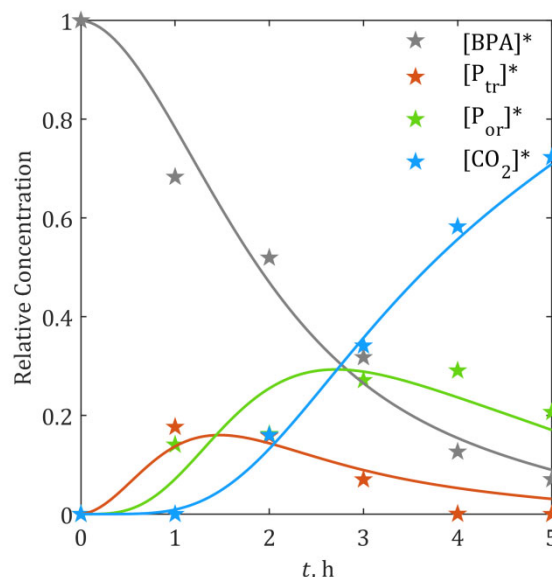


**Figure 4.** Estimation results of rate constants  $k_S$ ,  $k_B$  and  $k_M$ : ★—experimental data, solid lines—model predictions. Asterisk (\*) denotes normalized (relative) concentration.

## 2.5. Generalization and Validation of the Model for Different Current Densities

The kinetic model was generalized to predict BPA degradation efficiency across a range of current densities (2.5–20 mA/cm<sup>2</sup>). To establish the current density/rate constant dependence, we incorporated experimental data from Simić et al. [49] while maintaining determined values for the second-order rate constants ( $k_S = 1.002 \cdot 10^{10} \text{ 1/(M} \cdot \text{s)}$ ,  $k_B = 3.920 \cdot 10^{10} \text{ 1/(M} \cdot \text{s)}$ ,  $k_M = 1.387 \cdot 10^{10} \text{ 1/(M} \cdot \text{s)}$ ).

The proportionality factor  $k$ , governing relative  $\bullet\text{OH}$  concentrations in Equations (20), (22) and (23), exhibited a strong linear correlation with applied current density ( $R^2 = 0.989$ ). As shown in Figure 5a, this relationship follows  $k(j) = (6.48 \cdot 10^{-12} \text{ cm}^2/\text{mA}) \cdot j + 8.55 \cdot 10^{-12}$ , where  $j$  represents current density. Integration of this linear dependence into the kinetic model yielded simulated [BPA]\* profiles that closely matched experimental observations across all tested current densities (Figure 5b).

Model validation was focused on BPA removal efficiency due to the lack of intermediate concentration data. The statistical profile presented in Table 2 demonstrates robust predictive capability, with relative prediction errors (RMSE) below 10% and residual variance (RSS) under 5% across the current density range. Notably, the model showed particularly strong performance at higher current densities (10–20 mA/cm<sup>2</sup>), achieving an average  $R^2 \approx 0.97$  with  $\text{RMSE} \approx 5.66\%$  and  $\text{RSS} \approx 1.95\%$ . At 15 mA/cm<sup>2</sup> specifically, the results showed excellent agreement with Figure 4 data, with minimal deviations in determination coefficient ( $\Delta R^2 = 1.22\%$ ) and moderate increases in prediction error ( $\Delta \text{RMSE} = 5.37\%$ ) and residual variance ( $\Delta \text{RSS} = 11.04\%$ ).

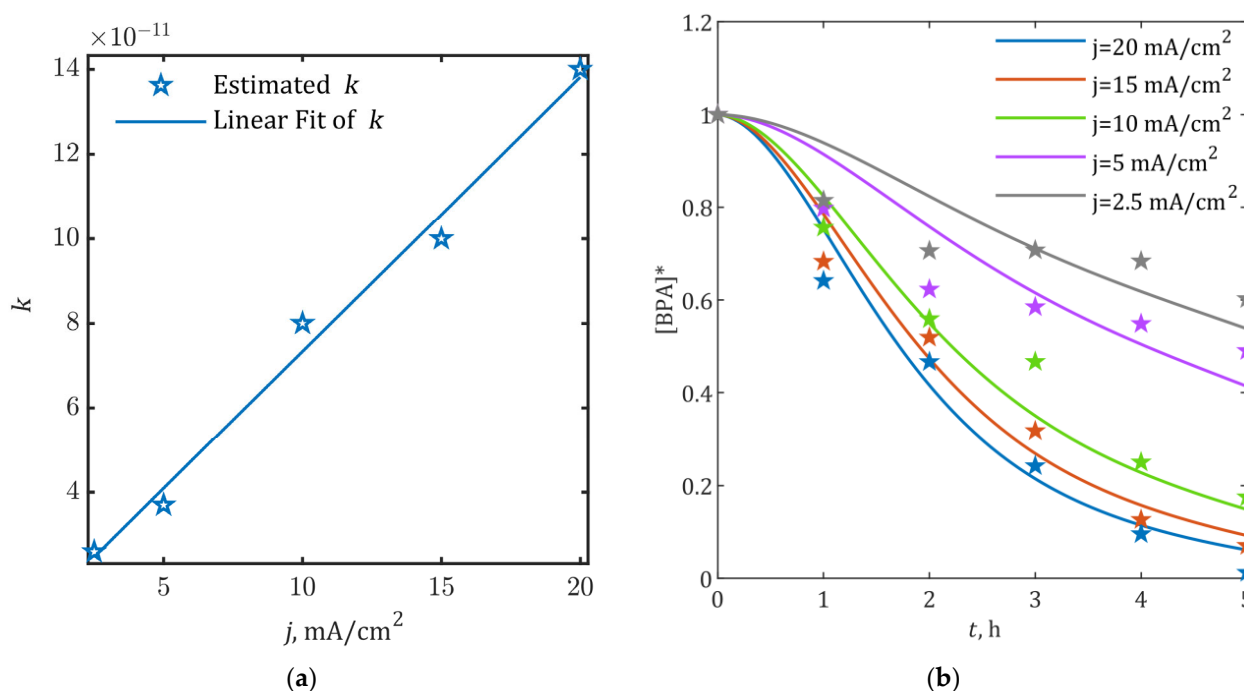


**Figure 5.** Current-density-dependent model performance: (a) Linear correlation between proportionality factor  $k$  and applied current density  $j$ ; (b) Comparison of simulated and experimental  $[\text{BPA}]^*$  profiles across current densities ( $2.5\text{--}20 \text{ mA}/\text{cm}^2$ ): ★—experimental data, solid lines—model predictions.

**Table 2.** Statistical evaluation of current-density-dependent model predictions for BPA removal efficiency. Metrics include determination coefficient ( $R^2$ ), root mean square error (RMSE), and residual sum of squares (RSS) for each tested current density ( $j$ ).

$j, \text{mA}/\text{cm}^2$	$R^2$	RMSE, 1	RSS, 1
20	0.9623	0.0659	0.0260
15	0.9712	0.0549	0.0181
10	0.9700	0.0491	0.0144
5	0.7536	0.0863	0.0447
2.5	0.6157	0.0786	0.0371

The predictive potential of the model ( $R^2$ ) decreases significantly for lower currents of  $2.5$  and  $5 \text{ mA}/\text{cm}^2$ , especially in the first stage of the process, likely due to the inability of low currents to assure irreversible electron transfer. On the other hand, reversibility of the processes (Equations (3)–(5)) was not taken into account in the present model, as the backwards rate constants were neglected for simplicity and clarity.

The model's maintained accuracy across varying operational conditions confirms its utility for predicting BPA degradation efficiency under different electrochemical treatment scenarios. This current-density-dependent generalized model can serve as both a design tool (predicting  $j$ -dependent efficiency) and a safety factor (quantified error bounds) for process optimization or potential scale-up applications.

## 2.6. Prediction of Intermediate Concentration and Toxicity Profiles at Different Current Densities

The temporal evolution concentration profile was predicted across current densities ( $2.5\text{--}20 \text{ mA}/\text{cm}^2$ ) using the kinetic model. Figure 6 presents the simulated concentration profiles of aromatic intermediates and  $\text{CO}_2$ , excluding  $15 \text{ mA}/\text{cm}^2$  data (previously shown in Figures 3b and 4) for clarity. The corresponding  $\bullet\text{OH}$  radical concentration profiles are presented in Figure S3.

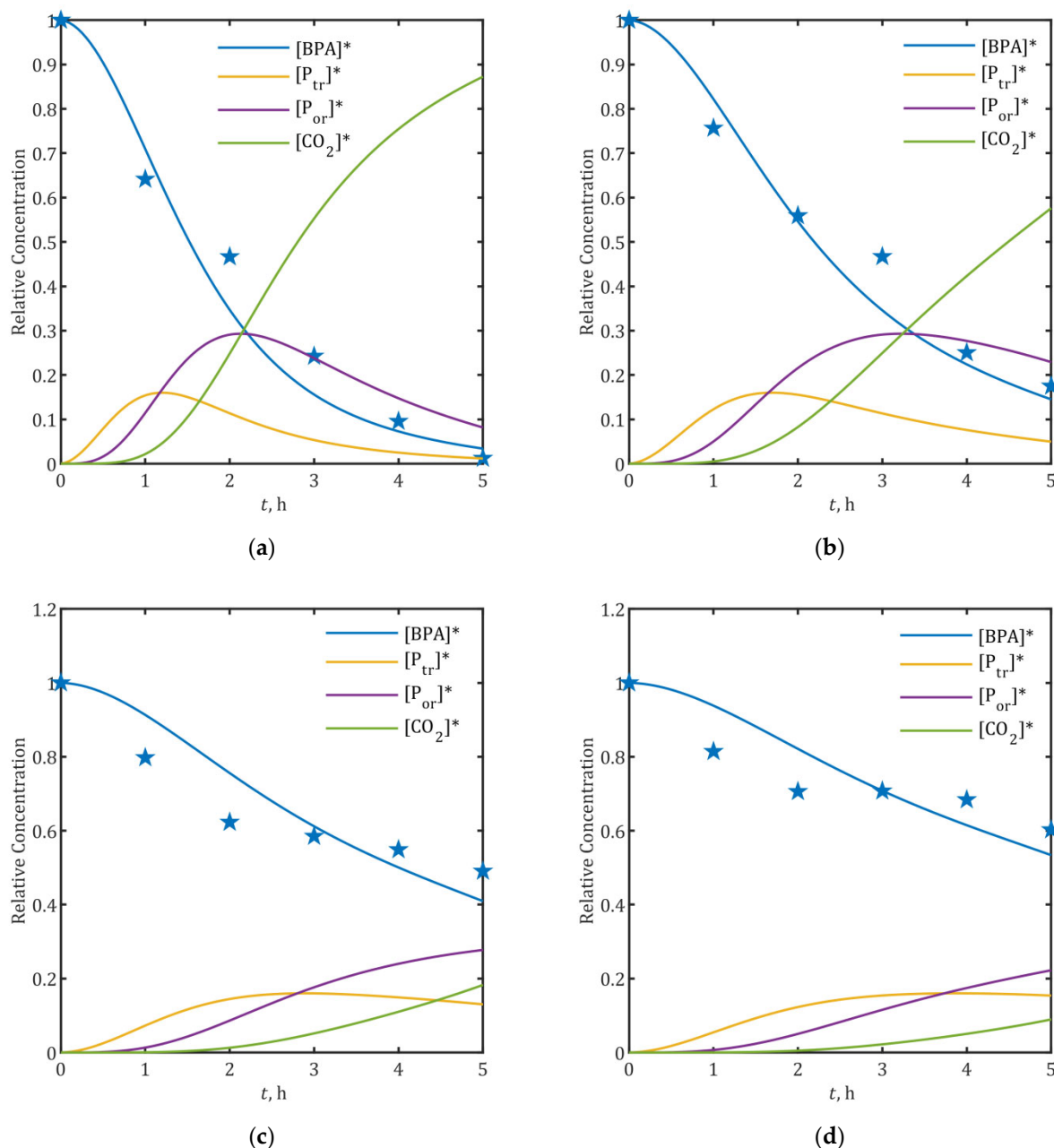


**Figure 6.** Simulated temporal profiles of BPA\*, degradation intermediates ( $P_{tr}^*$ ,  $P_{or}^*$ ), and  $CO_2^*$  during 5-h electrolysis at: (a) 20 mA/cm<sup>2</sup>; (b) 10 mA/cm<sup>2</sup>; (c) 5 mA/cm<sup>2</sup>; and (d) 2.5 mA/cm<sup>2</sup>. Experimental data are marked with star symbols (★), while solid lines represent model predictions.

The model predicts that after 5 h of electrolysis, successful degradation of both two-ring ( $P_{tr}$ ) and one-ring ( $P_{or}$ ) intermediates can only be achieved at 20 mA/cm<sup>2</sup> (Figure 6a). While 10 mA/cm<sup>2</sup> treatment effectively degraded more than 90% of  $P_{tr}$ ,  $P_{or}$  degradation remained negligible (Figure 6b). Lower current densities ( $\leq 5$  mA/cm<sup>2</sup>) showed limited treatment efficiency, with less than 60% BPA removal, negligible  $P_{tr}$  degradation ( $<1\%$ ), and net accumulation of  $P_{or}$  accompanied by low mineralization ( $\leq 20\%$ ).

The developed model successfully predicted temporal toxicity trends in the investigated system, with validation performed against experimental data at 15 mA/cm<sup>2</sup>. As illustrated in Figure 7, the simulated toxicity profile shows strong agreement with experimental results, achieving a determination coefficient of  $R^2 = 0.971$ .

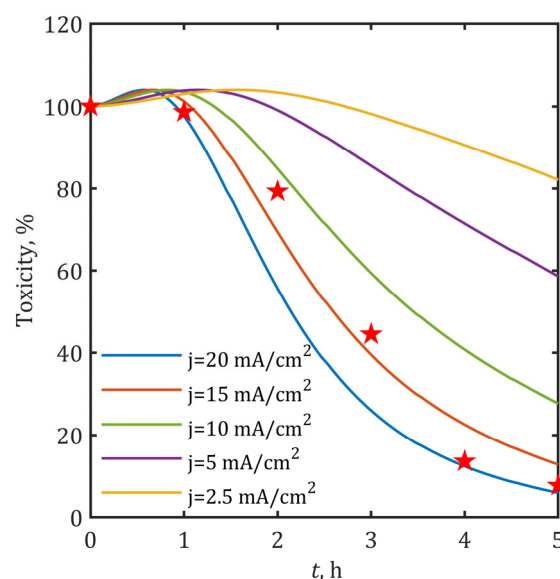


**Figure 7.** Current-density-dependent model predictions for SnO<sub>2</sub>-MWCNT@SS anode performance: normalized toxicity evolution (%) of treated solutions across applied current densities (2.5–20 mA/cm<sup>2</sup>) during 5-h BPA electrooxidation. Experimental data are marked with star symbols (★), while solid lines represent model predictions.

Predicted toxicity trends (Figure 7) reveal critical process dynamics. Toxicity evolution exhibited three distinct phases: (i) an initial 1–3% increase during the first 1–2 h, (ii) a maximum toxicity point, followed by (iii) a rapid decrease. This transition occurred earlier at higher current densities, completing after 1 h at 20 mA/cm<sup>2</sup> compared to 2 h at 2.5 mA/cm<sup>2</sup>. The rate of toxicity reduction scales with energy input, requiring > 10 mA/cm<sup>2</sup> to achieve > 80% toxicity reduction within 5 h. These results demonstrate that while partial BPA removal occurs at lower current densities, effective toxicity control requires sufficient •OH generation rates only achieved at ≥10 mA/cm<sup>2</sup>.

This biphasic toxicity profile aligns with the proposed reaction mechanism, where initial oxidation and formation of two-ring products generate more toxic fragments before their degradation to less harmful one-ring products and eventual mineralization up to CO<sub>2</sub> and water [37]. The findings underscore the importance of optimizing treatment parameters (current density and duration) to navigate the transient toxicity window while achieving maximal detoxification.

### 2.7. Generalizability Assessment for •OH-Mediated Electrochemical Oxidation of Organic Pollutants

The model operates on the premise that •OH radicals serve as the dominant reactive species for BPA degradation, an assumption supported by our earlier radical quenching experiments [49] and literature evidence confirming •OH-mediated aromatic ring attack as the primary pathway [50,51,67]. To assess the model's broader utility, we applied it to rhodamine B degradation [48], using experimental data obtained with the specific SnO<sub>2</sub>-MWCNT@SS anode system (initial concentration 1.04·10<sup>−4</sup> M, 50 ppm; pH ≈ 7; current density 20 mA/cm<sup>2</sup> over 3 h). UV-Vis spectroscopy served as the analytical method for rhodamine B quantification.

The •OH generation capacity of the electrode, characterized in Figure 5a, yielded a proportionality factor  $k = 1.38 \cdot 10^{-10}$ . The degradation pathway for rhodamine B was constructed based on identified intermediates and the mechanism proposed by Dai et al. [68], beginning with cleavage of the conjugated structure to form one-ring mono- and di-carboxylic acids (benzoic acid and its derivatives lumped as P<sub>1</sub>) and

followed by aromatic ring opening to produce aliphatic acids (succinic acid and 2-hydroxyglutaric acid lumped as  $P_2$ ) that are mineralized to  $\text{CO}_2$  and  $\text{H}_2\text{O}$ . Kinetic parameters were assigned with  $k_s = 9 \cdot 10^9 \text{ l}/(\text{M} \cdot \text{s})$  for the initial rhodamine B oxidation [69–71] and  $k_B = k_M = 1.2 \cdot 10^{10} \text{ l}/(\text{M} \cdot \text{s})$  for subsequent intermediate oxidation [72,73], based on literature values for structurally similar compounds (salicylic acid).

Model predictions demonstrated strong correlation with experimental data ( $R^2 = 0.961$ ), as shown in Figure 8, though minor discrepancies during the initial hour suggest the possible existence of transient alternative degradation pathways that become negligible as mineralization progresses. The predicted 20% mineralization efficiency aligns with established literature showing that while decolorization may be extensive, organic matter removal (TOC) often remains below 40% [74,75]. These results validate the model's reliability in predicting both degradation kinetics of principal pollutants and mineralization efficiency across operationally relevant conditions (different classes of organic pollutants; initial concentrations: 30–50 ppm; pH: 4–7;  $j > 10 \text{ mA}/\text{cm}^2$ ), despite its simplified reaction framework (Supplementary Materials Table S3). Given that short-duration electrooxidation (0–1 h) yields insufficient degradation/mineralization (<30%, Figures 4, 6 and 8) while generating more toxic intermediates than the parent pollutants (Figure 7), the model's predictive capability for longer treatment times—when process efficiency becomes practically significant—remains fully valid and operationally relevant.

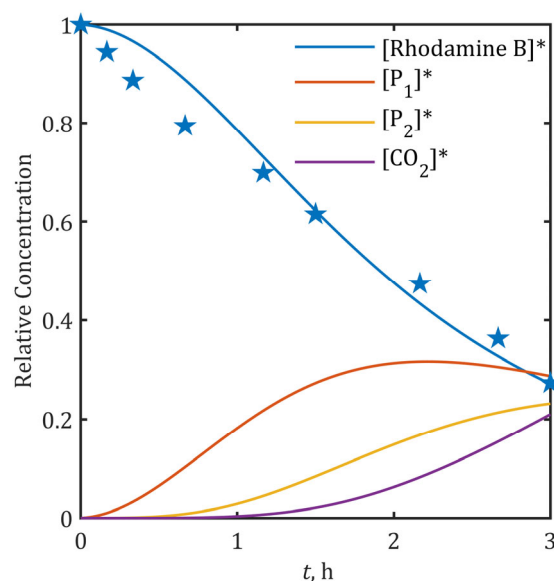


**Figure 8.** Experimental vs. predicted rhodamine B degradation kinetics at  $20 \text{ mA}/\text{cm}^2$ . Experimental data are marked with star symbols (★), while solid lines represent model predictions. Asterisk (\*) denotes normalized (relative) concentration.

### 3. Discussion

The concentration of  $\bullet\text{OH}$  radicals was estimated using equilibrium conditions and an easily measurable concentration of  $\text{H}_2\text{O}_2$ , one of the competitive water electrolysis products. The presented semiempirical methodology enables quantification and prediction of  $\bullet\text{OH}$  radical concentration, the key electrochemical variable in anodic oxidation experiments, being difficult to trace directly [9]. Moreover, when the  $\text{H}_2\text{O}_2$  measuring experiment is once performed, it enables insight into  $\bullet\text{OH}$ -radical concentration and the predictive estimation of the whole concentration profile of one-ring and two-ring products, even in the absence of GC/MS detection. The results show that once the proportionality factor between  $\bullet\text{OH}$  radical and  $\text{H}_2\text{O}_2$  concentrations is defined (Equation (20)), the model successfully predicts the concentration distribution of the pollutant based on its initial concentration and second-

order rate constant towards  $\bullet\text{OH}$  radicals. The proposed strategy enables the prediction of the complete electrooxidation process outcome, including degradation efficiency extent and toxicity time profile, using only simple data obtained from  $\text{H}_2\text{O}_2$  measurements within anodic oxidation experiments and available toxicity databases.

The presented estimation procedure includes assessment of the oxidative breakdown of BPA, identifying its key intermediates, and projecting the degradation pathway over a five-hour period of electrochemical oxidation. Based on these results, two crucial steps in the degradation process were identified. The first involves the oxidation of the BPA aliphatic backbone without breaking the chain, while the second entails the direct cleavage of the BPA molecule, yielding one-ring products. Ultimately, the process is proposed to result in the opening of rings and production of diverse aliphatic molecules, which are further oxidized to  $\text{CO}_2$  and  $\text{H}_2\text{O}$ , as corroborated by the obtained high degrees of complete mineralization.

The model was verified against previously published data on BPA degradation at different current densities. The validated linear relationship between  $\bullet\text{OH}$  availability and applied current density (Figure 5a) enables predictive control of degradation efficiency across operational scales, while the robust error margins (Table 2) establish reliability boundaries for engineering implementation. The procedure provided a correlation between process efficiency and energy input, emphasizing the uniformity and applicability of the model, at least at the current densities higher than  $10 \text{ mA/cm}^2$ . These currents enable satisfactory energy input for irreversible electron transfer, so the reversibility of the oxidation reactions can be neglected.

This current-density-dependent generalization provides both fundamental insights and practical tools for (1) optimizing electrooxidation conditions and (2) facilitating potential scale-up applications. The developed kinetic model can predict the concentration profiles of  $\bullet\text{OH}$  radicals, the principal pollutant, and its primary intermediate and product. It can also be used to assess process operational parameters such as treatment duration and applied current density, with the purpose of optimization of energy consumption. In connection with the computational databases on the toxicity, as demonstrated in the case of T.E.S.T. (Toxicity Estimation Software Tool), it can be used to estimate the toxicity of the degradation mixture and determine optimal operational conditions for the degradation to minimize toxicity, once all potentially toxic degradation by-products are known. As corroborated by obtained correlation coefficients, the model is particularly applicable for predicting the concentration profile of initial pollutants, the mineralization extents, and the relative toxicity. The prediction of the formation and depletion of intermediates in the tracked system was primarily qualitative, however, with the clear perspective for further improvement of precision. Through comprehensive characterization of oxidative intermediates, the lumping-based classification scheme can be systematically refined to enable precise toxicity predictions from simulated concentration profiles, as demonstrated by Ferreiro et al. in their study of UV/ $\text{H}_2\text{O}_2$ -mediated 4-chlorophenol degradation [37].

Finally, the results suggest that the model, which has a principally general character regarding chemical properties of involved species (Figure 8), can be widened to include other reactive species, if necessary more specifically defined. This would allow more complex kinetic studies of anodic oxidation or related  $\text{H}_2\text{O}_2$  mediated EAOPs processes [35].

## 4. Materials and Methods

### 4.1. Electrochemical Oxidation

The  $\text{SnO}_2$ -MWCNT@SS anode modeled in this study was prepared as described in our prior work [49], with essential procedural details summarized below. The  $\text{SnO}_2$ /MWCNT nanocomposite was synthesized by dispersing  $\text{SnO}_2$  nanoparticles with functionalized



multi-walled carbon nanotubes (MWCNTs, dimensions: 7–15 nm × 3–6 nm × 0.5–200 µm; Sigma-Aldrich, St. Louis, MO, USA) in dimethylformamide (DMF, Sigma-Aldrich, St. Louis, MO, USA) at a 3.5:1 (*w/w*) ratio. The mixture was sonicated for 5 h at room temperature to achieve a homogeneous suspension (4.5 mg/mL). A total of ~210 µL suspension (70 µL per application) was drop-cast onto a stainless steel substrate (1 × 2 cm, 2 cm<sup>2</sup> surface area) in three sequential layers, with each layer dried for 20 min under a 250 W infrared lamp. As validated in [49], structural and electrochemical characterization confirmed uniform nanocomposite distribution, stable anode performance, and enhanced electroactive surface area.

Bisphenol A (BPA, Sigma-Aldrich, St. Louis, MO, USA) degradation was investigated in a two-electrode electrochemical cell containing 60 mL of 0.1 M Na<sub>2</sub>SO<sub>4</sub> electrolyte with 1.31 · 10<sup>−4</sup> M BPA (30 ppm, pH ≈ 4). The system utilized an SnO<sub>2</sub>-MWCNT@SS working electrode and a stainless steel counter electrode. Chronopotentiometric experiments were performed for 5 h using a Gamry Interface 1000 Potentiostat/Galvanostat (Gamry Instruments, Warminster, PA, USA), with 0.5 mL aliquots collected at 1-h intervals for subsequent analysis. While reference [49] reported BPA degradation across multiple current densities (2.5–20 mA/cm<sup>2</sup>), this study focused exclusively on 15 mA/cm<sup>2</sup> for mechanistic analysis.

Aliquots were subjected to two parallel analytical workflows. GC-MS analysis (Agilent 7890B/5977A, Agilent Technologies, Inc., Santa Clara, CA, USA) enabled quantification of BPA degradation kinetics and identification of reaction intermediates. The measurement descriptions relevant to this study are provided in Text S3 (Supplementary Materials). Simultaneously, UV-Vis spectroscopy (Lambda 35, Perkin Elmer, Waltham, MA, USA) monitored H<sub>2</sub>O<sub>2</sub> formation via the titanium oxalate method [76], capturing its competitive generation alongside •OH radicals during water electrolysis. This dual-method approach provided comprehensive insight into both organic pollutant degradation and oxidant production dynamics. Total organic carbon (TOC) measurements were performed using a TOC-LCPH analyzer (Shimadzu Co., Kyoto, Japan) to quantify mineralization efficiency through the reduction in organic carbon content during electrooxidation.

#### 4.2. Time-Dependent Toxicity Profiling During BPA Electrooxidation

Acute toxicity of BPA and its degradation intermediates was evaluated using the United States Environmental Protection Agency's (U.S. EPA's) Toxicity Estimation Software Tool (T.E.S.T., version 5.1.2) with the Consensus quantitative structure-activity relationship (QSAR) model. Toxicity was expressed as LC<sub>50</sub> values, representing the aqueous concentration (mg/L) causing 50% mortality in Fathead Minnow (*Pimephales promelas*) after 96-h exposure.

The temporal toxicity profile was derived from the relative acute toxicities of BPA and its pseudo-intermediates (two-ring derivatives P<sub>tr</sub> and one-ring derivatives P<sub>or</sub>), calculated as

$$\text{Toxicity}(\%) = 100 \cdot \frac{\text{LC}_{50\text{BPA}}}{M_{\text{BPA}}} \cdot \sum_i \frac{[i]^*}{\text{LC}_{50i}/M_i} = 100 \cdot \text{LC}_{50\text{BPA}}^* \cdot \sum_i \frac{[i]^*}{\text{LC}_{50i}^*} \quad (24)$$

where *i* denotes BPA, P<sub>tr</sub> and P<sub>or</sub>, and LC<sub>50BPA</sub> is the reference toxicity value. LC<sub>50i</sub> represents the acute toxicity of individual components (BPA, P<sub>tr</sub> and P<sub>or</sub>), and M<sub>i</sub> denotes their corresponding molar masses. The full derivation of these relationships is provided in Supplementary Materials (Text S4).

#### 4.3. Mathematical Modelling

Model parameters were estimated using experimental data from BPA electrooxidation at 15 mA/cm<sup>2</sup> with the SnO<sub>2</sub>-MWCNT@SS anode, including temporal profiles of

relative concentrations for BPA, degradation intermediates ( $P_{tr}$  and  $P_{or}$ ),  $H_2O_2$ , and  $CO_2$ . For validation, independent datasets of BPA degradation at additional current densities (5–20 mA/cm<sup>2</sup>) from [49] were employed.

Parameter optimization was implemented in MATLAB® (The MathWorks, Inc., Natick, MA, USA [77]) via the Optimization Toolbox™ lsqcurvefit function [78], utilizing a trust-region-reflective algorithm to solve the nonlinear least-squares problem [79,80]. Process simulations were performed using the ode45 solver [81], which implements an explicit Runge-Kutta fourth- and fifth-order method for nonstiff differential equations [82,83].

**Supplementary Materials:** The following supporting information can be downloaded at: <https://www.mdpi.com/article/10.3390/ijms26104785/s1>.

**Author Contributions:** Conceptualization, M.J.D. and D.V.A.; methodology, M.J.D., T.B. and D.V.A.; validation, L.Š., B.B. and R.P.; formal analysis, M.J.D. and D.A.; investigation, M.J.D. and D.A.; resources, L.Š. and T.B.; data curation, L.Š. and M.J.D.; writing—original draft preparation, M.J.D., D.V.A. and T.B.; writing—review and editing, L.Š., B.B. and R.P.; visualization, D.A., L.Š. and R.P.; supervision, B.B. and T.B.; project administration, L.Š. and T.B.; funding acquisition, D.V.A. and T.B. All authors have read and agreed to the published version of the manuscript.

**Funding:** This research was funded by the Ministry of Science, Technological Development, and Innovation of the Republic of Serbia, grant number 451-03-136/2025-03/200017.

**Institutional Review Board Statement:** Not applicable.

**Informed Consent Statement:** Not applicable.

**Data Availability Statement:** The original contributions presented in this study are included in the article/Supplementary Materials. Further inquiries can be directed to the corresponding authors.

**Acknowledgments:** This work was supported by the Ministry of Science, Technological Development, and Innovation of the Republic of Serbia [grant numbers 451-03-136/2025-03/200017 and 451-03-136/2025-03/200135]. Ľubomír Švorc would like to thank the Scientific Grant Agency of the Ministry of Education of the Slovak Republic and the Slovak Academy of Sciences [grant number VEGA No. 1/0036/24] and the Slovak Research and Development Agency under the Contract No. APVV-23-0066.

**Conflicts of Interest:** The authors declare no conflicts of interest. The funders had no role in the design of the study; in the collection, analyses, or interpretation of data; in the writing of the manuscript; or in the decision to publish the results.

## Abbreviations

The following abbreviations are used in this manuscript.

	Letter designations
AOPs	Advanced oxidation processes
BPA	Bisphenol A
EAOPs	Electrochemical advanced oxidation processes
EF	Electro-Fenton process
EO	Electrooxidation process
EPR	Electron paramagnetic resonance spectroscopy
$HO_2\bullet$	Hydroperoxyl radicals
$\bullet OH$	Hydroxyl radical
$P_{or}$	Lumped one-ring BPA degradation intermediates
$P_{tr}$	Lumped two-ring BPA degradation intermediates
$P_1$	Lumped aromatic rhodamine B degradation intermediates
$P_2$	Lumped aliphatic rhodamine B degradation intermediates

SnO <sub>2</sub> -MWCNT@SS	Tin oxide/multi-walled carbon nanotube composite on stainless steel substrate
SO <sub>4</sub> • <sup>−</sup>	Sulfate radical
T.E.S.T.	U.S. EPA's toxicity estimation software tool
	Physical Quantities
[BPA] <sub>0</sub>	Initial BPA concentration (M)
B <sub>0</sub>	Zero-order polynomial coefficient for H <sub>2</sub> O <sub>2</sub> fit (dimensionless)
B <sub>1</sub>	First-order polynomial coefficient for H <sub>2</sub> O <sub>2</sub> fit (1/s)
B <sub>2</sub>	Second-order polynomial coefficient for H <sub>2</sub> O <sub>2</sub> fit (1/s <sup>2</sup> )
B <sub>3</sub>	Third-order polynomial coefficient for H <sub>2</sub> O <sub>2</sub> fit (1/s <sup>3</sup> )
[i] <sub>t</sub>	Time-dependent concentration of species i = BPA, P <sub>tr</sub> , P <sub>or</sub> , CO <sub>2</sub> , •OH, H <sub>2</sub> O <sub>2</sub> (M)
[i]*	Relative concentration of species i = BPA, P <sub>tr</sub> , P <sub>or</sub> , CO <sub>2</sub> , •OH, H <sub>2</sub> O <sub>2</sub> (dimensionless)
j	Current density (mA/cm <sup>2</sup> )
k	Proportionality factor (dimensionless)
k <sub>•OH</sub> <sup>pollutant</sup>	Pseudo-second-order rate constant of •OH radicals with pollutants (1/(M·s))
k <sub>B</sub>	Second-order rate constant for P <sub>tr</sub> cleavage (1/(M·s))
k <sub>M</sub>	Second-order rate constant for P <sub>or</sub> mineralization (1/(M·s))
k <sub>S</sub>	Second-order rate constant for BPA degradation (1/(M·s))
k <sub>B</sub> <sup>*</sup>	Normalized rate constant for P <sub>tr</sub> cleavage (dimensionless)
k <sub>M</sub> <sup>*</sup>	Normalized rate constant for P <sub>or</sub> mineralization (dimensionless)
k <sub>S</sub> <sup>*</sup>	Normalized rate constant for BPA degradation (dimensionless)
LC <sub>50</sub>	96-h acute toxicity for <i>Pimephales promelas</i> (Fathead Minnow) (mg/L)
M	Molar mass (g/mol)
R <sup>2</sup>	Coefficient of determination (dimensionless)
RMSE	Root mean square error (units match predicted variable)
RSS	Residual sum of squares (matches the square of the predicted variable's units)
t	Time (s)
t*	Scaled time (dimensionless)
TOC	Total organic carbon content (mg/L)
V	System volume (L)
	Mathematical Operators
Δ	Difference operator
Σ	Summation operator

## References

1. Vinayagam, V.; Palani, K.N.; Ganesh, S.; Rajesh, S.; Akula, V.V.; Avoodaiappan, R.; Kushwaha, O.S.; Pugazhendhi, A. Recent Developments on Advanced Oxidation Processes for Degradation of Pollutants from Wastewater with Focus on Antibiotics and Organic Dyes. *Environ. Res.* **2024**, *240*, 117500. [[CrossRef](#)] [[PubMed](#)]
2. Brdarić, T.P.; Aćimović, D.D.; Švorc, L.; Vasić Aničijević, D.D. Bibliometric Study of Electrochemical Advanced Oxidation Processes (EAOPs) for Wastewater Treatment. *Coatings* **2024**, *14*, 1060. [[CrossRef](#)]
3. Hübner, U.; Spahr, S.; Lutze, H.; Wieland, A.; Rüting, S.; Gernjak, W.; Wenk, J. Advanced Oxidation Processes for Water and Wastewater Treatment—Guidance for Systematic Future Research. *Heliyon* **2024**, *10*, e30402. [[CrossRef](#)]
4. Zhang, L.; Peng, W.; Wang, W.; Cao, Y.; Fan, G.; Huang, Y.; Qi, M. A Comprehensive Review of the Electrochemical Advanced Oxidation Processes: Detection of Free Radical, Electrode Materials and Application. *J. Environ. Chem. Eng.* **2024**, *12*, 113778. [[CrossRef](#)]
5. Liu, G.; Tian, Y.; Zou, H.; Ren, N.; You, S. Thermodynamic and Kinetic Investigation on Electrogenation of Hydroxyl Radicals for Water Purification. *ACS EST Eng.* **2023**, *3*, 2161–2170. [[CrossRef](#)]
6. Özcan, A.; Şahin, Y.; Koparal, A.S.; Oturan, M.A. Protham Mineralization in Aqueous Medium by Anodic Oxidation Using Boron-Doped Diamond Anode: Influence of Experimental Parameters on Degradation Kinetics and Mineralization Efficiency. *Water Res.* **2008**, *42*, 2889–2898. [[CrossRef](#)]
7. Cai, J.; Zhou, M.; Pan, Y.; Du, X.; Lu, X. Extremely Efficient Electrochemical Degradation of Organic Pollutants with Co-Generation of Hydroxyl and Sulfate Radicals on Blue-TiO<sub>2</sub> Nanotubes Anode. *Appl. Catal. B Environ.* **2019**, *257*, 117902. [[CrossRef](#)]

8. Kuang, C.; Zeng, G.; Zhou, Y.; Wu, Y.; Li, D.; Wang, Y.; Li, C. Integrating Anodic Sulfate Activation with Cathodic H<sub>2</sub>O<sub>2</sub> Production/Activation to Generate the Sulfate and Hydroxyl Radicals for the Degradation of Emerging Organic Contaminants. *Water Res.* **2023**, *229*, 119464. [\[CrossRef\]](#)
9. Xie, J.; Zhang, C.; Waite, T.D. Hydroxyl Radicals in Anodic Oxidation Systems: Generation, Identification and Quantification. *Water Res.* **2022**, *217*, 118425. [\[CrossRef\]](#)
10. Fu, R.; Zhang, P.-S.; Jiang, Y.-X.; Sun, L.; Sun, X.-H. Wastewater Treatment by Anodic Oxidation in Electrochemical Advanced Oxidation Process: Advance in Mechanism, Direct and Indirect Oxidation Detection Methods. *Chemosphere* **2023**, *311*, 136993. [\[CrossRef\]](#)
11. Dai, M.; Niu, Q.; Wu, S.; Lin, Y.; Biswas, J.K.; Yang, C. Hydroxyl Radicals in Ozone-Based Advanced Oxidation of Organic Contaminants: A Review. *Environ. Chem. Lett.* **2024**, *22*, 3059–3106. [\[CrossRef\]](#)
12. Bielski, B.H.J.; Cabelli, D.E.; Arudi, R.L.; Ross, A.B. Reactivity of HO<sub>2</sub>/O<sup>−</sup><sub>2</sub> Radicals in Aqueous Solution. *J. Phys. Chem. Ref. Data* **1985**, *14*, 1041–1100. [\[CrossRef\]](#)
13. Neta, P.; Huie, R.E.; Ross, A.B. Rate Constants for Reactions of Inorganic Radicals in Aqueous Solution. *J. Phys. Chem. Ref. Data* **1988**, *17*, 1027–1284. [\[CrossRef\]](#)
14. Buxton, G.V.; Greenstock, C.L.; Helman, W.P.; Ross, A.B. Critical Review of Rate Constants for Reactions of Hydrated Electrons, Hydrogen Atoms and Hydroxyl Radicals (·OH/·O<sup>−</sup> in Aqueous Solution. *J. Phys. Chem. Ref. Data* **1988**, *17*, 513–886. [\[CrossRef\]](#)
15. Cao, Y.; Yao, J.; Knudsen, T.Š.; Pang, W.; Zhu, J.; Liu, B.; Li, H.; Li, M.; Su, J. Radical Chemistry, Degradation Mechanism and Toxicity Evolution of BPA in the UV/Chlorine and UV/H<sub>2</sub>O<sub>2</sub>. *Chemosphere* **2023**, *312*, 137169. [\[CrossRef\]](#)
16. Luo, Z.; Yan, Y.; Spinney, R.; Dionysiou, D.D.; Villamena, F.A.; Xiao, R.; Vione, D. Environmental Implications of Superoxide Radicals: From Natural Processes to Engineering Applications. *Water Res.* **2024**, *261*, 122023. [\[CrossRef\]](#)
17. Alanazi, M.; Yong, J.; Wu, M.; Zhang, Z.; Tian, D.; Zhang, R. Recent Advances in Detection of Hydroxyl Radical by Responsive Fluorescence Nanoprobes. *Chem.—Asian J.* **2024**, *19*, e202400105. [\[CrossRef\]](#)
18. Braxton, E.; Fox, D.J.; Breeze, B.G.; Tully, J.J.; Levey, K.J.; Newton, M.E.; Macpherson, J.V. Electron Paramagnetic Resonance for the Detection of Electrochemically Generated Hydroxyl Radicals: Issues Associated with Electrochemical Oxidation of the Spin Trap. *ACS Meas. Sci. Au* **2022**, *3*, 21–31. [\[CrossRef\]](#)
19. Barroso-Martínez, J.S.; Romo, A.I.B.; Pudar, S.; Putnam, S.T.; Bustos, E.; Rodríguez-López, J. Real-Time Detection of Hydroxyl Radical Generated at Operating Electrodes via Redox-Active Adduct Formation Using Scanning Electrochemical Microscopy. *J. Am. Chem. Soc.* **2022**, *144*, 18896–18907. [\[CrossRef\]](#)
20. Roberts, J.G.; Voinov, M.A.; Schmidt, A.C.; Smirnova, T.I.; Sombers, L.A. The Hydroxyl Radical Is a Critical Intermediate in the Voltammetric Detection of Hydrogen Peroxide. *J. Am. Chem. Soc.* **2016**, *138*, 2516–2519. [\[CrossRef\]](#)
21. Hu, Y.-L.; Lu, Y.; Zhou, G.-J.; Xia, X.-H. A Simple Electrochemical Method for the Determination of Hydroxyl Free Radicals without Separation Process. *Talanta* **2008**, *74*, 760–765. [\[CrossRef\]](#) [\[PubMed\]](#)
22. Minakata, D. Development of an Elementary Reaction-Based Kinetic Model to Predict the Aqueous-Phase Fate of Organic Compounds Induced by Reactive Free Radicals. *Acc. Chem. Res.* **2024**, *57*, 1658–1669. [\[CrossRef\]](#)
23. Fu, J.; Li, H.; Jiang, G.; Feng, D.; Yi, J.; Liu, Y.; Gong, R.; Guo, J.; Liu, P.; Cui, K. Enhanced Removal of Tetracycline Hydrochloride by Activation of Persulfate with Sludge-Red Mud Magnetic Biochar: Synergistic Effect between Adsorption and Radical-Nonradical Pathways. *Inorg. Chem. Commun.* **2024**, *170*, 113451. [\[CrossRef\]](#)
24. Ziola, A.C.; Ziemann, P.J. Effects of a Carboxyl Group on the Products, Mechanism, and Kinetics of the OH Radical-Initiated Oxidation of 3-Butenoic Acid Under Low NO<sub>x</sub> Conditions. *J. Phys. Chem. A* **2025**, *129*, 1688–1703. [\[CrossRef\]](#) [\[PubMed\]](#)
25. Mandel, P.; Roche, P.; Wolbert, D. Large-Scale Experimental Validation of a Model for the Kinetics of Ozone and Hydroxyl Radicals with Natural Organic Matter. *Ozone Sci. Eng.* **2014**, *36*, 73–85. [\[CrossRef\]](#)
26. Zhang, Y.; Guo, L.; Hoffmann, M.R. Ozone- and Hydroxyl Radical-Mediated Oxidation of Pharmaceutical Compounds Using Ni-Doped Sb-SnO<sub>2</sub> Anodes: Degradation Kinetics and Transformation Products. *ACS Est Eng.* **2023**, *3*, 335–348. [\[CrossRef\]](#)
27. Liu, H.; Li, X.Z.; Leng, Y.J.; Wang, C. Kinetic Modeling of Electro-Fenton Reaction in Aqueous Solution. *Water Res.* **2007**, *41*, 1161–1167. [\[CrossRef\]](#)
28. Groenen-Serrano, K.; Weiss-Hortala, E.; Savall, A.; Spiteri, P. Role of Hydroxyl Radicals During the Competitive Electrooxidation of Organic Compounds on a Boron-Doped Diamond Anode. *Electrocatalysis* **2013**, *4*, 346–352. [\[CrossRef\]](#)
29. Turchi, C.S.; Ollis, D.F. Photocatalytic Degradation of Organic Water Contaminants: Mechanisms Involving Hydroxyl Radical Attack. *J. Catal.* **1990**, *122*, 178–192. [\[CrossRef\]](#)
30. Yazdani, E.B.; Mehrizad, A. Sonochemical Preparation and Photocatalytic Application of Ag-ZnS-MWCNTs Composite for the Degradation of Rhodamine B under Visible Light: Experimental Design and Kinetics Modeling. *J. Mol. Liq.* **2018**, *255*, 102–112. [\[CrossRef\]](#)
31. Wols, B.A.; Harmsen, D.J.H.; Wanders-Dijk, J.; Beerendonk, E.F.; Hofman-Caris, C.H.M. Degradation of Pharmaceuticals in UV (LP)/H<sub>2</sub>O<sub>2</sub> Reactors Simulated by Means of Kinetic Modeling and Computational Fluid Dynamics (CFD). *Water Res.* **2015**, *75*, 11–24. [\[CrossRef\]](#)



32. Luo, S.; Gao, L.; Wei, Z.; Spinney, R.; Dionysiou, D.D.; Hu, W.-P.; Chai, L.; Xiao, R. Kinetic and Mechanistic Aspects of Hydroxyl Radical-mediated Degradation of Naproxen and Reaction Intermediates. *Water Res.* **2018**, *137*, 233–241. [\[CrossRef\]](#)
33. Takahashi, Y.; Kobayashi, M.; Kawase, Y. Photocatalytic Degradation Process of Antibiotic Sulfamethoxazole by ZnO in Aquatic Systems: A Dynamic Kinetic Model Based on Contributions of OH Radical, Oxygenated Radical Intermediates and Dissolved Oxygen. *J. Environ. Sci. Health Part A* **2024**, *59*, 113–124. [\[CrossRef\]](#) [\[PubMed\]](#)
34. Ateia, M.; Alalm, M.G.; Awfa, D.; Johnson, M.S.; Yoshimura, C. Modeling the Degradation and Disinfection of Water Pollutants by Photocatalysts and Composites: A Critical Review. *Sci. Total Environ.* **2020**, *698*, 134197. [\[CrossRef\]](#) [\[PubMed\]](#)
35. Nakagawa, H.; Takagi, S.; Maekawa, J. Fered-Fenton Process for the Degradation of 1,4-Dioxane with an Activated Carbon Electrode: A Kinetic Model Including Active Radicals. *Chem. Eng. J.* **2016**, *296*, 398–405. [\[CrossRef\]](#)
36. Sun, M.; Liu, H.-H.; Zhang, Y.; Zhai, L.-F. Degradation of Bisphenol A by Electrocatalytic Wet Air Oxidation Process: Kinetic Modeling, Degradation Pathway and Performance Assessment. *Chem. Eng. J.* **2020**, *387*, 124124. [\[CrossRef\]](#)
37. Ferreira, C.; Sanz, J.; Villota, N.; de Luis, A.; Lombraña, J.I. Kinetic Modelling for Concentration and Toxicity Changes during the Oxidation of 4-Chlorophenol by UV/H<sub>2</sub>O<sub>2</sub>. *Sci. Rep.* **2021**, *11*, 15726. [\[CrossRef\]](#)
38. Koli, M.; Kanwar, B.; Singh, S.P. Impact of Operating Parameters on the Electrooxidation of Methylene Blue and Ciprofloxacin: A Comprehensive Analysis and Degradation Pathway. *Environ. Sci. Pollut. Res.* **2025**, *32*, 4656–4669. [\[CrossRef\]](#)
39. Song, Z.; Wu, X.; Gao, T.; Yao, F.; Tang, X.; Mahmood, Q.; Tang, C.-J. Performance Enhancement Strategies for Electrooxidation Degradation of Landfill Leachate: A Review. *Chin. Chem. Lett.* **2025**, 111008. [\[CrossRef\]](#)
40. Pignatello, J.J.; Oliveros, E.; MacKay, A. Advanced Oxidation Processes for Organic Contaminant Destruction Based on the Fenton Reaction and Related Chemistry. *Crit. Rev. Environ. Sci. Technol.* **2006**, *36*, 1–84. [\[CrossRef\]](#)
41. Balseviciute, A.; Patiño-Cantero, I.; Carrillo-Abad, J.; Giner-Sanz, J.J.; García-Gabaldón, M.; Pérez-Herranz, V.; Martí-Calatayud, M.C. Degradation of Multicomponent Pharmaceutical Mixtures by Electrochemical Oxidation: Insights about the Process Evolution at Varying Applied Currents and Concentrations of Organics and Supporting Electrolyte. *Sep. Purif. Technol.* **2025**, *362*, 131697. [\[CrossRef\]](#)
42. PubChem. Bisphenol A. Available online: <https://pubchem.ncbi.nlm.nih.gov/compound/6623> (accessed on 19 June 2024).
43. Li, L.; Zhang, H.; Liu, Z.; Su, Y.; Du, C. Adsorbent Biochar Derived from Corn Stalk Core for Highly Efficient Removal of Bisphenol A. *Environ. Sci. Pollut. Res.* **2023**, *30*, 74916–74927. [\[CrossRef\]](#) [\[PubMed\]](#)
44. Sun, J.; Tong, L.; Shen, S.; Chen, Z.; Zhang, Z.; Gong, B.; Cui, L.; He, Y.; Huang, Z. Electrochemical Oxidation of Bisphenol A with a Fe-N-C/Persulfate Three-Dimensional Electrochemical System. *J. Environ. Chem. Eng.* **2024**, *12*, 114245. [\[CrossRef\]](#)
45. Zhang, Q.; Wu, C.-Z.; Huang, Z.; Liu, Y.; Hong, J. Electrochemical Treatment of Bisphenol a Facilitated by a Dual-Ligand Copper Metal-Organic Framework/Graphene Oxide Hybrid Catalyst. *J. Environ. Chem. Eng.* **2025**, *13*, 116243. [\[CrossRef\]](#)
46. Sharma, J.; Mishra, I.M.; Kumar, V. Mechanistic Study of Photo-Oxidation of Bisphenol-A (BPA) with Hydrogen Peroxide (H<sub>2</sub>O<sub>2</sub>) and Sodium Persulfate (SPS). *J. Environ. Manag.* **2016**, *166*, 12–22. [\[CrossRef\]](#)
47. Kaplan, R.; Erjavec, B.; Senila, M.; Pintar, A. Catalytic Wet Air Oxidation of Bisphenol A Solution in a Batch-Recycle Trickle-Bed Reactor over Titanate Nanotube-Based Catalysts. *Environ. Sci. Pollut. Res.* **2014**, *21*, 11313–11319. [\[CrossRef\]](#)
48. Ječmenica Dučić, M.; Aćimović, D.; Savić, B.; Rakočević, L.; Simić, M.; Brdarić, T.; Vasić Anićijević, D. Is It Possible to Restrain OER on Simple Carbon Electrodes to Efficiently Electrooxidize Organic Pollutants? *Molecules* **2022**, *27*, 5203. [\[CrossRef\]](#)
49. Simić, M.D.; Savić, B.G.; Ognjanović, M.R.; Stanković, D.M.; Relić, D.J.; Aćimović, D.D.; Brdarić, T.P. Degradation of Bisphenol A on SnO<sub>2</sub>-MWCNT Electrode Using Electrochemical Oxidation. *J. Water Process Eng.* **2023**, *51*, 103416. [\[CrossRef\]](#)
50. Cui, Y.; Li, X.; Chen, G. Electrochemical Degradation of Bisphenol A on Different Anodes. *Water Res.* **2009**, *43*, 1968–1976. [\[CrossRef\]](#)
51. Wu, W.; Huang, Z.-H.; Lim, T.-T. A Comparative Study on Electrochemical Oxidation of Bisphenol A by Boron-Doped Diamond Anode and Modified SnO<sub>2</sub>-Sb Anodes: Influencing Parameters and Reaction Pathways. *J. Environ. Chem. Eng.* **2016**, *4*, 2807–2815. [\[CrossRef\]](#)
52. Han, Q.; Wang, M.; Sun, F.; Yu, B.; Dong, Z.; Li, P.; Luo, J.; Li, M.; Jin, X.; Dai, Z. Effectiveness and Degradation Pathways of Bisphenol A (BPA) Initiated by Hydroxyl Radicals and Sulfate Radicals in Water: Initial Reaction Sites Based on DFT Prediction. *Environ. Res.* **2023**, *216*, 114601. [\[CrossRef\]](#) [\[PubMed\]](#)
53. Ding, J.; Bu, L.; Zhao, Q.; Kabutey, F.T.; Wei, L.; Dionysiou, D.D. Electrochemical Activation of Persulfate on BDD and DSA Anodes: Electrolyte Influence, Kinetics and Mechanisms in the Degradation of Bisphenol A. *J. Hazard. Mater.* **2020**, *388*, 121789. [\[CrossRef\]](#)
54. Kundu, S.; Das, B.K.; Wodeyar, A.; Majumder, P.; Jana, S.; Biswas, A.; Das, S.; Besra, R. Clearing the Path: Unraveling Bisphenol a Removal and Degradation Mechanisms for a Cleaner Future. *J. Environ. Manag.* **2025**, *373*, 123558. [\[CrossRef\]](#) [\[PubMed\]](#)
55. Darsinou, B.; Frontistis, Z.; Antonopoulou, M.; Konstantinou, I.; Mantzavinos, D. Sono-Activated Persulfate Oxidation of Bisphenol A: Kinetics, Pathways and the Controversial Role of Temperature. *Chem. Eng. J.* **2015**, *280*, 623–633. [\[CrossRef\]](#)
56. PubChem. PubChem. Available online: <https://pubchem.ncbi.nlm.nih.gov/> (accessed on 28 March 2025).

57. Simić, M.D.; Brdarić, T.P.; Savić Rosić, B.G.; Švorc, L.; Relić, D.J.; Aćimović, D.D. Degradation of Bisphenol A via the Electro-Fenton Process Using Nanostructured Carbon-Metal Oxide Anodes: Intermediates and Reaction Mechanisms Study. *J. Environ. Chem. Eng.* **2024**, *12*, 113369. [CrossRef]
58. Poerschmann, J.; Trommler, U.; Górecki, T. Aromatic Intermediate Formation during Oxidative Degradation of Bisphenol A by Homogeneous Sub-Stoichiometric Fenton Reaction. *Chemosphere* **2010**, *79*, 975–986. [CrossRef]
59. Kusvuran, E.; Yildirim, D. Degradation of Bisphenol A by Ozonation and Determination of Degradation Intermediates by Gas Chromatography–Mass Spectrometry and Liquid Chromatography–Mass Spectrometry. *Chem. Eng. J.* **2013**, *220*, 6–14. [CrossRef]
60. Lu, N.; Lu, Y.; Liu, F.; Zhao, K.; Yuan, X.; Zhao, Y.; Li, Y.; Qin, H.; Zhu, J. H3PW12O40/TiO<sub>2</sub> Catalyst-Induced Photodegradation of Bisphenol A (BPA): Kinetics, Toxicity and Degradation Pathways. *Chemosphere* **2013**, *91*, 1266–1272. [CrossRef]
61. Gözmen, B.; Oturan, M.A.; Oturan, N.; Erbatur, O. Indirect Electrochemical Treatment of Bisphenol A in Water via Electrochemically Generated Fenton's Reagent. *Environ. Sci. Technol.* **2003**, *37*, 3716–3723. [CrossRef]
62. Mandal, S. Reaction Rate Constants of Hydroxyl Radicals with Micropollutants and Their Significance in Advanced Oxidation Processes. *J. Adv. Oxid. Technol.* **2018**, *21*, 20170075. [CrossRef]
63. Lin, Z.; Qin, W.; Sun, L.; Yuan, X.; Xia, D. Kinetics and Mechanism of Sulfate Radical- and Hydroxyl Radical-Induced Degradation of Bisphenol A in VUV/UV/Peroxymonosulfate System. *J. Water Process Eng.* **2020**, *38*, 101636. [CrossRef]
64. Kondrakov, A.O.; Ignatev, A.N.; Frimmel, F.H.; Bräse, S.; Horn, H.; Revelsky, A.I. Formation of Genotoxic Quinones during Bisphenol A Degradation by TiO<sub>2</sub> Photocatalysis and UV Photolysis: A Comparative Study. *Appl. Catal. B Environ.* **2014**, *160–161*, 106–114. [CrossRef]
65. Xiao, R.; Gao, L.; Wei, Z.; Spinney, R.; Luo, S.; Wang, D.; Dionysiou, D.D.; Tang, C.; Yang, W. Mechanistic Insight into Degradation of Endocrine Disrupting Chemical by Hydroxyl Radical: An Experimental and Theoretical Approach. *Environ. Pollut.* **2017**, *231*, 1446–1452. [CrossRef]
66. Gao, J.; Duan, X.; O'Shea, K.; Dionysiou, D.D. Degradation and Transformation of Bisphenol A in UV/Sodium Percarbonate: Dual Role of Carbonate Radical Anion. *Water Res.* **2020**, *171*, 115394. [CrossRef]
67. Xie, Z.-H.; He, C.-S.; Zhou, H.-Y.; Li, L.-L.; Liu, Y.; Du, Y.; Liu, W.; Mu, Y.; Lai, B. Effects of Molecular Structure on Organic Contaminants' Degradation Efficiency and Dominant ROS in the Advanced Oxidation Process with Multiple ROS. *Environ. Sci. Technol.* **2022**, *56*, 8784–8795. [CrossRef] [PubMed]
68. Dai, Q.; Jiang, L.; Luo, X. Electrochemical Oxidation of Rhodamine B: Optimization and Degradation Mechanism. *Int. J. Electrochem. Sci.* **2017**, *12*, 4265–4276. [CrossRef]
69. Zhang, Y.; Luo, G.; Wang, Q.; Zhang, Y.; Zhou, M. Kinetic Study of the Degradation of Rhodamine B Using a Flow-through UV/Electro-Fenton Process with the Presence of Ethylenediaminetetraacetic Acid. *Chemosphere* **2020**, *240*, 124929. [CrossRef]
70. Ferguson, M.W.; Beaumont, P.C.; Jones, S.E.; Navaratnam, S.; Parsons, B.J. Excited State and Free Radical Properties of Rhodamine 123: A Laser Flash Photolysis and Radiolysis Study. *Phys. Chem. Chem. Phys.* **1999**, *1*, 261–268. [CrossRef]
71. Navaratnam, S.; Parsons, B.J. Kinetic and Spectral Properties of Rhodamine 6G Free Radicals: A Pulse Radiolysis Study. *J. Photochem. Photobiol. Chem.* **2002**, *153*, 153–162. [CrossRef]
72. Amphlett, C.B.; Adams, G.E.; Michael, B.D. Pulse Radiolysis Studies of Deaerated Aqueous Salicylate Solutions. In *Radiation Chemistry; Advances in Chemistry*; American Chemical Society: Washington, DC, USA, 1968; Volume 81, pp. 231–250, ISBN 978-0-8412-0082-1.
73. Guinea, E.; Arias, C.; Cabot, P.L.; Garrido, J.A.; Rodríguez, R.M.; Centellas, F.; Brillas, E. Mineralization of Salicylic Acid in Acidic Aqueous Medium by Electrochemical Advanced Oxidation Processes Using Platinum and Boron-Doped Diamond as Anode and Cathodically Generated Hydrogen Peroxide. *Water Res.* **2008**, *42*, 499–511. [CrossRef]
74. Li, Q.; Zhang, Q.; Cui, H.; Ding, L.; Wei, Z.; Zhai, J. Fabrication of Cerium-Doped Lead Dioxide Anode with Improved Electrocatalytic Activity and Its Application for Removal of Rhodamine B. *Chem. Eng. J.* **2013**, *228*, 806–814. [CrossRef]
75. Benvenuti, T.; Gabriel, A.P.; Heberle, A.N.A.; Lucena, M.P.P.; Petter, P.M.H.; Meneguzzi, Á.; Bernardes, A.M. Evaluation of direct photolysis, electrooxidation and photoelectrooxidation for Rhodamine-B degradation. *Braz. J. Chem. Eng.* **2018**, *35*, 957–968. [CrossRef]
76. Sellers, R.M. Spectrophotometric Determination of Hydrogen Peroxide Using Potassium Titanium(IV) Oxalate. *Analyst* **1980**, *105*, 950–954. [CrossRef]
77. Little, J.; Moler, C. *MATLAB*; MathWorks: Natick, MA, USA, 2023.
78. Solve Nonlinear Curve-Fitting (Data-Fitting) Problems in Least-Squares Sense—MATLAB Lsqcurvefit. Available online: [https://www.mathworks.com/help/optim/ug/lsqcurvefit.html?s\\_tid=srchtitle\\_site\\_search\\_1\\_lsqcurvefit](https://www.mathworks.com/help/optim/ug/lsqcurvefit.html?s_tid=srchtitle_site_search_1_lsqcurvefit) (accessed on 31 March 2024).
79. Coleman, T.F.; Li, Y. On the Convergence of Interior-Reflective Newton Methods for Nonlinear Minimization Subject to Bounds. *Math. Program.* **1994**, *67*, 189–224. [CrossRef]
80. Coleman, T.F.; Li, Y. An Interior Trust Region Approach for Nonlinear Minimization Subject to Bounds. *SIAM J. Optim.* **1996**, *6*, 418–445. [CrossRef]



81. Solve Nonstiff Differential Equations—Medium Order Method—MATLAB Ode45. Available online: <https://www.mathworks.com/help/matlab/ref/ode45.html> (accessed on 1 April 2024).
82. Dormand, J.R.; Prince, P.J. A Family of Embedded Runge-Kutta Formulae. *J. Comput. Appl. Math.* **1980**, *6*, 19–26. [[CrossRef](#)]
83. Shampine, L.F.; Reichelt, M.W. The MATLAB ODE Suite. *SIAM J. Sci. Comput.* **1997**, *18*, 1–22. [[CrossRef](#)]

**Disclaimer/Publisher’s Note:** The statements, opinions and data contained in all publications are solely those of the individual author(s) and contributor(s) and not of MDPI and/or the editor(s). MDPI and/or the editor(s) disclaim responsibility for any injury to people or property resulting from any ideas, methods, instructions or products referred to in the content.